APT and TEM Study of Behaviour of Alloying Elements in Neutron-Irradiated Zirconium-Based Alloys

Authors: B. M. Jenkins[1*], J. Haley[1*], M. P. Moody[1], J. M. Hyde[1,2], C. R. M. Grovenor[1]

[1] Department of Materials, University of Oxford, Parks Road, Oxford, OX1 3PH

[2] National Nuclear Laboratory, Building D5, First Floor, Culham Science Centre, Abingdon, Oxfordshire, OX14 3DB

Corresponding authors: benjamin.jenkins@materials.ox.ac.uk, jack.haley@materials.ox.ac.uk

Keywords:

atom probe tomography (APT), transmission electron microscopy (TEM), irradiation embrittlement, clustering, spinodal decomposition

Abstract:

In this study, APT and TEM analyses were used to characterise two Zr-based alloys neutron-irradiated to 13.7 dpa. The high spatial and chemical resolution of these techniques has enabled the irradiation-induced nanoscale distribution of solute elements to be characterised. The results on both Zircaloy-2 and low-Sn ZIRLO support previous observations of Fe segregation to planar dislocation arrays with enhanced Sn between. In Zircaloy-2, the APT data in this study have also revealed short-range (~2 nm) clustering of Fe and Sn atoms both within the Fe-enriched planes and in the regions between dislocation arrays. The resultant microstructure is reminiscent of spinodal decomposition. In low-Sn ZIRLO Nb-rich precipitates formed in the Sn-rich planes. The data in this article enhance our understanding of microstructural evolution in Zr alloys under neutron irradiation and are relevant for predicting changes in the properties of Zr alloys in-service in fission reactors.

Graphical Abstract:

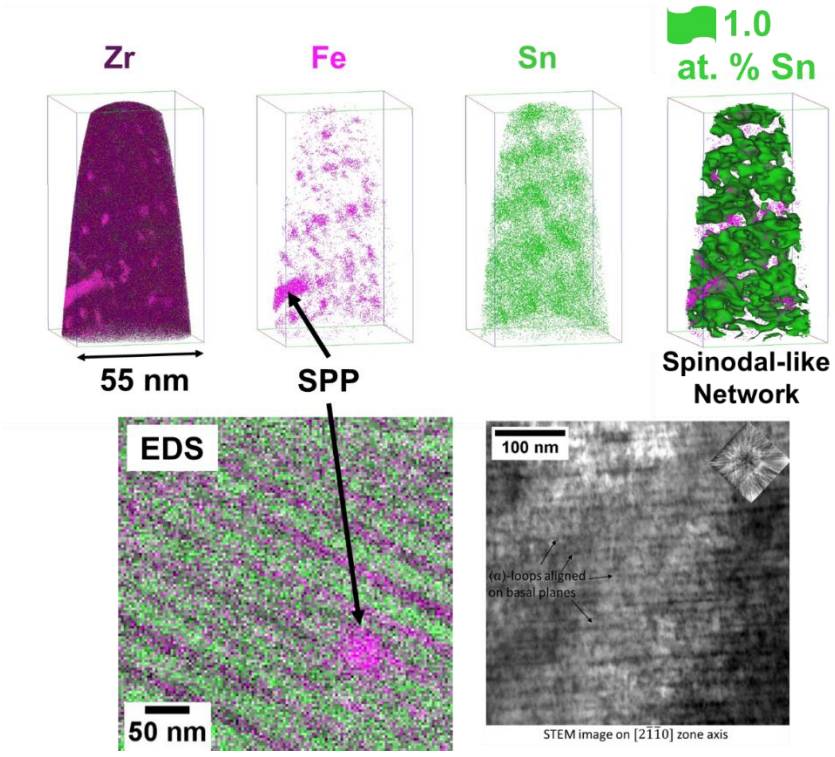

Main Text

Zirconium alloys used in Light Water Reactor (LWR) fuel assemblies are known to undergo a range of significant microstructural changes when exposed to neutron irradiation, including the formation of arrays of dislocation loops and precipitation/segregation of solute atoms [1]. This leads to severe changes to their mechanical properties, especially irradiation growth and embrittlement [2,3]. Nb-free alloys such as Zircaloy-2 exhibit much larger irradiation-induced swelling [4] than more recently developed Nb-containing counterparts like ZIRLO [5,6]. This irradiation-induced swelling limits the service lifetime of Zr-based fuel cladding in LWRs, and extending the time that fuel rods can safely operate has significant economic (reduced reactor downtime) and environmental (more complete fuel burn-up and less waste produced per GWh generated) benefits.

Accurate prediction of safe Zr-clad fuel rod lifetimes, and the design of novel Zr alloys to increase these lifetimes, relies upon a thorough understanding of the changes that these materials undergo as a result of exposure to the harsh environments experienced in reactor cores. A large body of work has been published on the generation of dislocation arrays under irradiation [7–9], and more recently on local chemical redistributions around these arrays, for instance the anti-correlation of Sn and Fe along the c-axis in Zircaloy-2 [9] and the formation of solute clusters on dislocation loops after irradiation [10–12]. Atomistic modelling indicates that Fe has a positive drag ratio with vacancies in Zr, whilst Sn has a negative drag ratio [13]; potentially explaining why Fe segregates to dislocation loops that act as sinks for vacancies. However, our understanding of solute behaviour in Zr alloys exposed to neutron irradiation, and its effect in a wider range of alloys, is still very limited.

Here we have used Atom Probe Tomography (APT), and Energy Dispersive X-ray Spectroscopy (EDS) in a Scanning Transmission Electron Microscope (STEM) to analyse the local chemistry changes occurring in heavily neutron-irradiated Zircaloy-2 and low-Sn ZIRLO. Use of these complementary techniques allows the microstructure to be characterised at different length scales, which is necessary to form a complete analysis of the local chemistry changes in the alloys.

The composition of the Zircaloy-2 and low-Sn ZIRLO alloys used in this study are given in Table 1. Both alloys were manufactured by Westinghouse, with slabs of each alloy initially hot rolled then beta quenched. Final dimensions were achieved via a series of cold-rolling passes. A final recrystallisation anneal was performed at 750 °C for 4 minutes for the Zircaloy-2, whilst the low-Sn ZIRLO underwent an anneal at 575 °C for 5 hours.

Table 1: Nominal composition (wt. %) of the Zr alloys analysed in this study.

Alloy	Nb	Sn	Fe	Ni	Cr	O
Zircaloy-2	<0.004	1.346	0.168	0.066	0.104	0.12
Low Sn ZIRLO	0.95	0.66	0.12	0.0036	0.0073	0.12

Both alloys were then neutron-irradiated in the BOR-60 reactor at 320 ± 10 °C up to a fluence of 16.2×10^{25} n/m^2, which is estimated to correspond to a damage level of 27 dpa [14]. Appreciable irradiation-induced swelling was observed for both alloys after exposure to irradiation, but was much more severe in the Zircaloy-2 [14].

APT and TEM specimens were prepared from the samples irradiated to 13.7 dpa using a FEI Helios NanoLab 600i Focussed Ion Beam at the UKAEA Materials Research Facility. Standard preparation APT and TEM procedures were followed [15–17], with a final FIB polishing stage conducted at 2 kV in an attempt to minimise Ga implantation into the APT specimens. TEM foils cleaned using 5 kV Ga^+ ions were preferable to those cleaned with 2 kV ions as they were found to contain less FIB-induced hydride, while retaining few FIB-induced dislocations.

APT analysis was conducted on a Cameca LEAP 5000 XR. Samples were analysed at a pulse frequency of 125 kHz in both laser- and voltage-pulsing modes; a base temperature of 60 K was used for laser-pulsing experiments and 70 K was used for voltage-pulsing experiments. A voltage pulse fraction of 20 % was applied, whilst a laser pulse energy of 80 pJ was used for one experiment (experimental parameters are specified in the figure captions). Reconstructions and analysis were performed in IVAS 3.8.8, with AtomProbeLab being used for compositional calculations [18,19].

STEM and EDS analysis was conducted using a JEOL ARM200F operating at 200 kV with a cold field emission source, and equipped with a JEOL 100mm^2 Centurion EDS detector. Qualitative elemental maps were produced using Hyperspy [20] and ImageJ [21], using simple windowing either side of the peaks of interest to estimate the contribution from bremsstrahlung X-rays. The elemental maps were constructed from the Kα lines for all elements except Sn, for which the Lα line was used due to the counts being too low for the Kα.

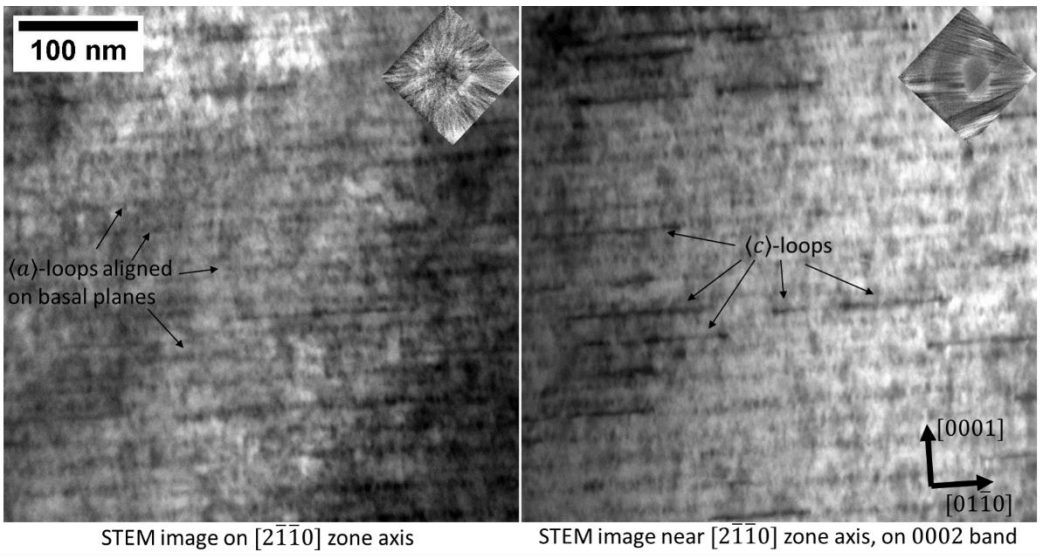

Figure 1: TEM micrographs revealing the dislocation structure in Zircaloy-2 after neutron-irradiation to 13.7 dpa. When the sample is oriented close to the [2$\bar{1}\bar{1}$0] zone axis, the <a>-loops show with strong diffraction contrast; when oriented off the zone axis and on the 0002 Kikuchi band, the <a>-loops have weaker contrast while the <c>-loops appear strong. The direction of [0001] is also indicated. Inserts on a) and b) depict the convergent beam diffraction pattern as an indication of the imaging condition for each image.

STEM analysis revealed a series of <a>-type dislocation loops aligned along the basal planes in the Zircaloy-2 (Figure 1), consistent with previous reports in proton and neutron-irradiated Zircaloy-2 [7,9,22]. The distribution of solute elements in the Zircaloy-2 is also observed to be highly heterogeneous after neutron irradiation. Clear segregation of Fe, Cr, and Sn, and a small Fe-Cr-rich secondary-phase particle, can be seen in the APT data in Figure 2 (a), and comparing these distributions with the arrays of <a>-loops in Figure 1, the Fe and Cr clusters are likely to be concentrated within the layers of dislocations on the basal plane. A 1D-concentration profile in the APT data taken perpendicularly to these planes indicates that Sn and Fe are anti-correlated on the length scale of approximately 15 nm - 20 nm (Figure 2 (c)), and the EDS results in Figure 2 (d and e) complement the APT results, with banding of Fe and Sn clearly observed on a slightly larger length scale (25 nm - 40 nm). This anti-correlation of Sn and Fe on the length-scale of ~50 nm has previously been seen in proton-irradiated Zircaloy-2 by Harte et al. [9].

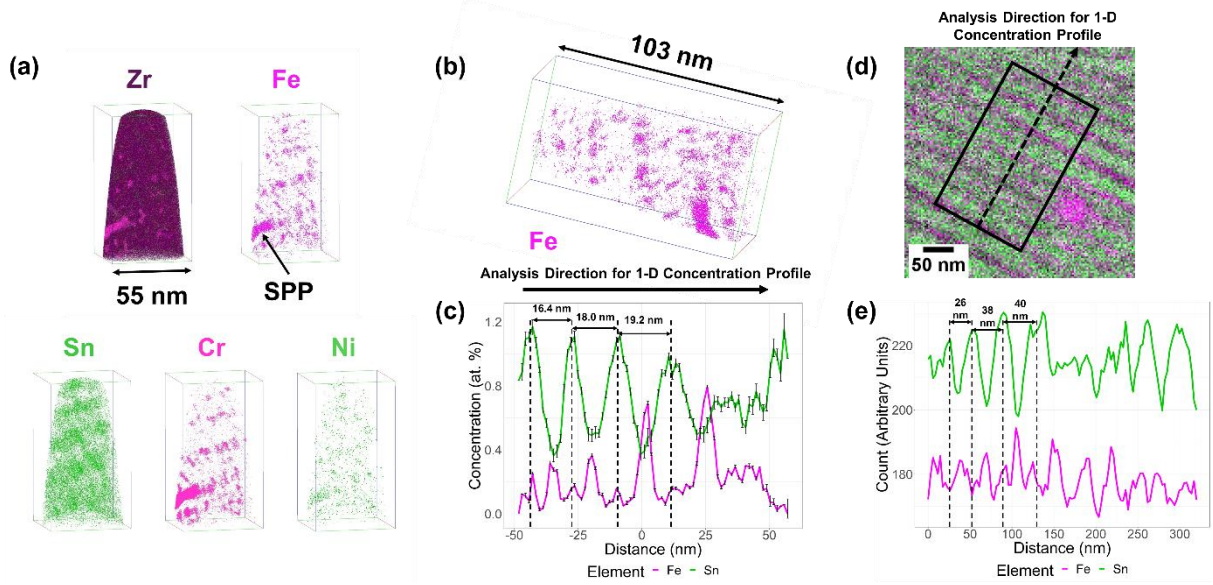

Figure 2: (a) Atom maps showing the distribution of Zr, Fe, Sn, Cr, and Ni in Zircaloy-2 irradiated to 13.7 dpa. (b) direction of 1-D concentration profile taken and (c) 1-D concentration profile demonstrating the variation in Sn and Fe concentration along this direction. (Dataset is from a voltage-pulse experiment and the bounding box has dimensions: 103 nm x 57 nm x 55 nm.) (d) EDS map showing the distribution of Sn and Fe atoms and the direction of the 1-D concentration profile across planes in EDS map that is shown in (e).

More detailed analysis of the APT data has revealed that the Sn and Fe are not wholly spatially anti-correlated. Figure 3 (b) shows the in-plane distribution of Sn and Fe within one of the dislocation arrays (high Fe, low Sn (~0.4 at.%)) in the dataset from Figure 2; whilst Figure 3 (c) contains a section between the dislocation arrays where the Sn concentration is much higher (~1.1 at. %) and the Fe concentration much lower (~0.1 at.%); it can be seen in both sections that there are regions enriched in Sn and Fe.

In addition, the Sn atoms in both Figure 3 (b) and Figure 3 (c) appear to form a 3D network, with well-defined Fe clusters located along this network. Figure 3 (d) is the detector event histogram for this dataset and shows the location of poles and zone lines; the Sn and Fe in Figure 3 (b) and Figure 3 (c) show no apparent correlation to these features, indicating that the observed spatial distribution of Sn and Fe is unlikely to be an artefact caused by surface migration, especially of Sn [23], as the voltage-pulsing analysis conditions used in this APT experiment should minimise this phenomenon.

Figure 3 (e) shows an isosurface generated at 1.0 at. % Sn for the section of the dataset shown in Figure 3 (c), revealing that the Sn forms a continuous network. A similar observation can be made for the section in Figure 3 (b), but since overall levels of Sn are lower in this region, the continuity of the Sn-rich regions is less well defined. Therefore, it appears that Sn and Fe are spatially correlated both within the Fe-rich plane of the dislocation arrays and in the Sn-rich planes between the dislocations. This co-clustering is not observed in the STEM EDS data; thus indicating the necessity of using characterisation techniques with different spatial resolutions to reveal all the details of the solute distributions in these alloys after irradiation.

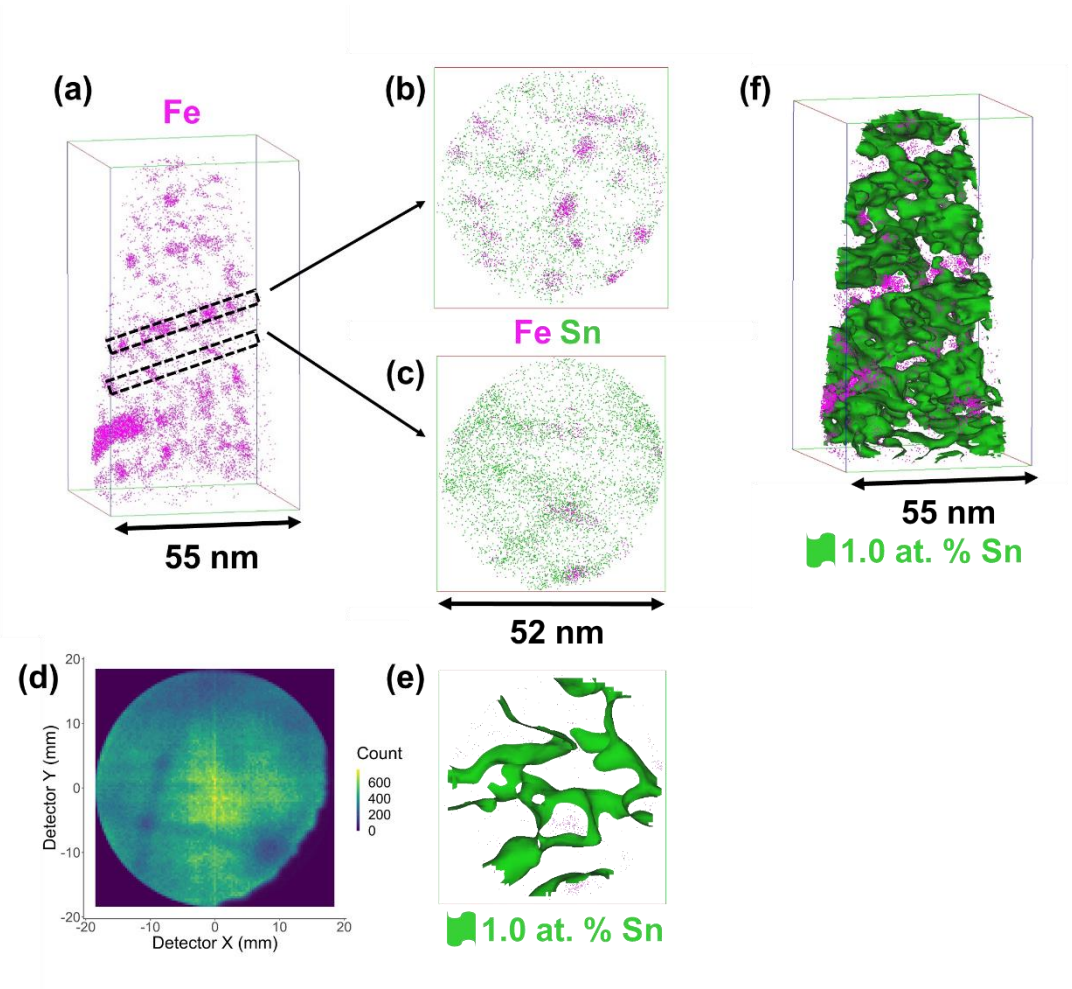

Figure 3: Atom maps showing (a) Fe location throughout the Zircaloy-2 APT dataset; (b) distribution of Fe and Sn within an 8 nm section of a dislocation array (enriched with Fe compared to the matrix); (c) distribution of Fe and Sn within a 8 nm section of plane between the dislocation arrays. (d) Shows the detector event histogram for the analysis and (e) represents the 1.0 at. % Sn isosurfaces generated for the section of the dataset shown in (c). (f) Isosurfaces generated at 1 at. % Sn throughout the whole dataset. (Dataset is from a voltage-pulse experiment and the bounding box has dimensions: 103 nm x 57 nm x 55 nm.)

When a Sn isosurface is generated for the entire dataset (Figure 3 (f)), there appears to be a continuous network of Sn-rich regions that, as well as being present where the Sn concentration is highest between the dislocation arrays, also links the Sn-rich regions together. This characteristic distribution is consistent with how spinodal decomposition has previously been observed in other material systems characterised with APT [24–26].

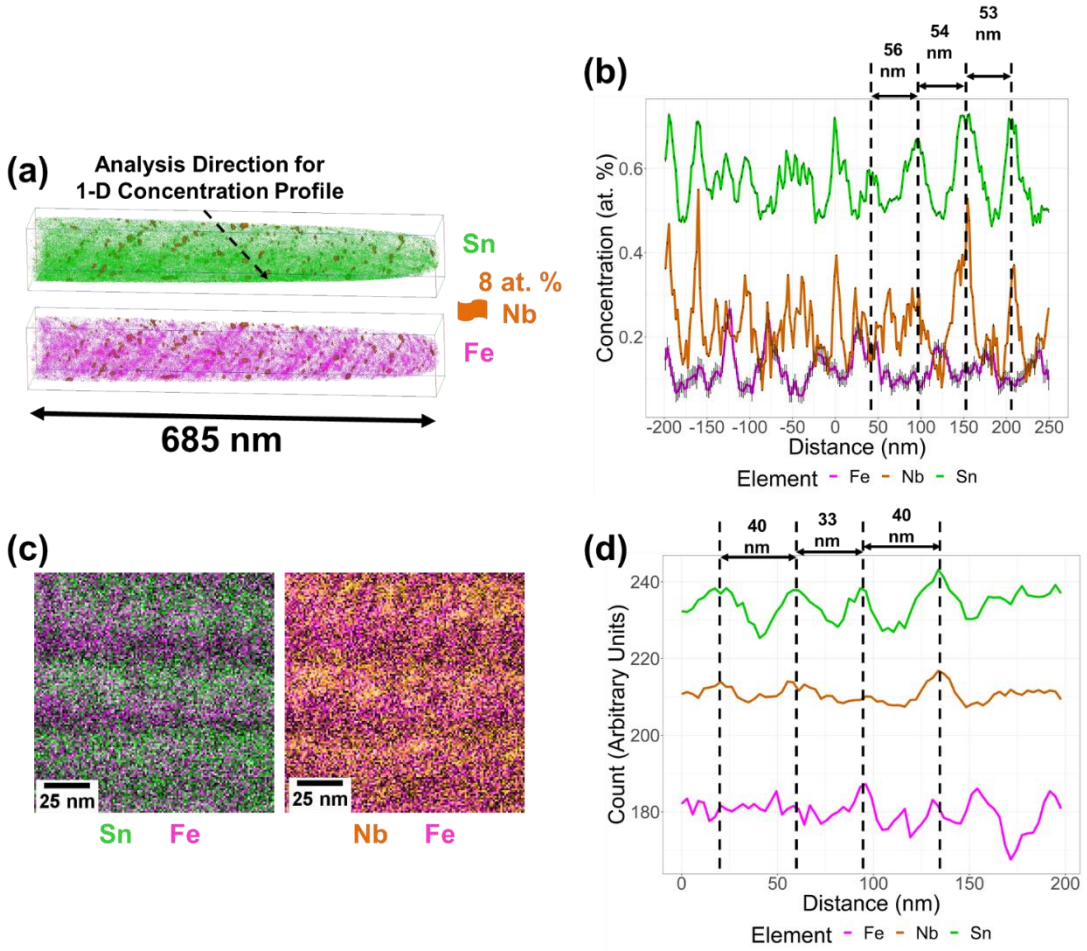

Figure 4 (a) Atom maps showing the location of Sn and Fe atoms in the Low-Sn ZIRLO after irradiation to 13.7 dpa. 8 at. % Nb isosurfaces are also displayed. (b) 1-D concentration profile taken from APT data perpendicularly to the dislocation arrays showing the variation in Sn, Nb, and Fe. (Dataset is from a laser-pulse experiment (80 pJ) and the bounding box has dimensions: 695 nm x 111 nm x 108 nm.) (c) STEM-EDS maps showing the Sn, Fe, and Nb distribution in the Low-Sn ZIRLO after irradiation to 13.7 dpa. (d) 1-D concentration profile taken from EDS data (N.B. the basal plane was misorientated from the imaging plane by approximately 10-15º).

Figure 4 shows APT and EDS results on the distribution of Sn, Fe and Nb in low-Sn ZIRLO after irradiation to 13.7 dpa. Similar to the Zircaloy-2 date above, Fe and Sn-rich regions have formed, whilst discrete Nb-rich precipitates have also formed in the Sn-rich planes. Similar Nb-rich precipitates have been observed in High Resolution Transmission Electron Micrographs from neutron-irradiated Zr-Nb alloys [8,27]. The Nb-rich nanoprecipitates in the low-Sn ZIRLO can just be resolved in the EDS maps in Figure 4 (c).

The 1-D concentration profile from the APT data (Figure 4 (b)) indicates that the Sn and Nb are correlated with one another and anti-correlated with Fe with a wavelength of ~ 55 nm, an observation not previously reported for irradiated Nb-containing Zr alloys. Because of the difference in the bulk composition of this alloy, the Fe and Sn levels are lower in this dataset than in the Zircaloy-2 data presented in Figure 2 (c), and the wavelength of the compositional fluctuations seems to be larger in the low-Sn ZIRLO. Whilst the EDS map in Figure 4 (c) qualitatively shows that Fe is anti-correlated with Sn and Nb, the 1-D concentration profile in Figure 4 (d) indicates that the anti-correlation of Fe in the STEM-EDS data is not as strong as that in the APT data and has a slightly shorter wavelength (30 nm – 40 nm). While the EDS maps shown for Zircaloy-2 were captured with the C-direction aligned normal to the beam direction, the C-direction in maps captured of the low-Sn ZIRLO

foil were not perfectly normal to the beam due to tilting limitations of the specimen holder. This would explain why the anti-correlation of Fe with Sn is not as strong as that seen in the same alloy by APT. The spacing between the Sn-rich planes, as measured by EDS and APT, is not consistent, with the slightly larger mean spacing in the APT data. EDS maps of both Zircaloy-2 and low-Sn ZIRLO have shown there is some variation in the band spacing across the sample, depending on proximity to SPPs (for example, Figure 2 (d)), and possibly other defects. The distance between dislocation arrays also varies along their length, and there is also likely to be grain-to-grain variations in this spacing. Since APT samples a much smaller volume of material than the TEM foils, this may explain these differences in the spacings measured by APT and STEM."

The 3-D distribution of solute atoms in the APT data in Figure 5 shows, similarly to the Zircaloy-2 data, that the Sn appears to form a complex, interconnected network that could be interpreted as spinodal decomposition in this alloy.

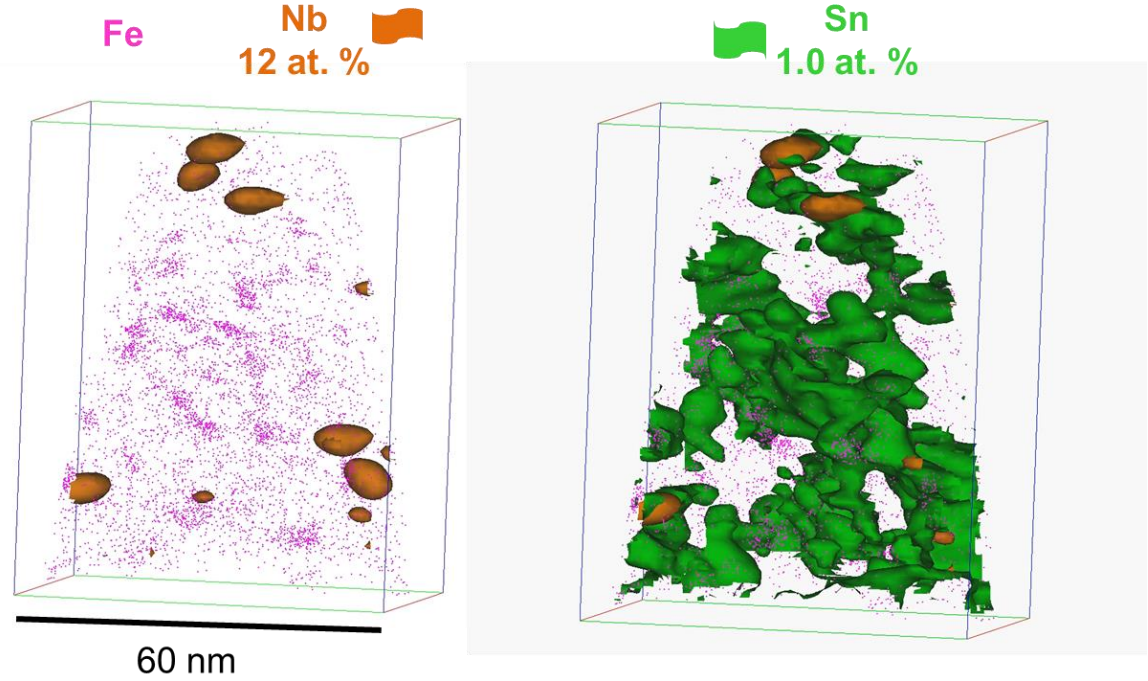

Figure 5 Atom maps showing the distribution of Fe, Nb, and Sn in the Low-Sn ZIRLO after irradiation to 13.7 dpa. (Dataset is from a voltage-pulse experiment and the bounding box has dimensions: 77 nm x 60 nm x 59 nm.).

APT and TEM analysis have been used to characterise two Zr alloys (one Nb-free and one Nb-containing) after exposure to neutron irradiation. These techniques provide complementary information on the complex nanostructural changes, especially the spatial distributions of the key solute elements Cr, Fe, Sn, and Nb that control the corrosion rates of these alloys. Fe and Sn were observed to anti-correlate, with Fe segregating to dislocation arrays and Sn segregating between the arrays. However, APT also revealed that Sn forms an intricate 3-D network in the Zircaloy-2, and that Fe is spatially correlated with this network in the regions between the dislocation arrays. In order to demonstrate that these observed solute distributions were a result of the irradiation, as-received samples were analysed using APT. Samples from both alloys demonstrated uniform solute distribution in their as-received state and atom maps showing this are included in the supplementary material.

The complex 3-D network of Sn is consistent with previous observations of spinodal decomposition in other alloys. However, the Zr-Sn binary phase diagram does not exhibit spinodal decomposition and so further research is necessary to determine if spinodal

decomposition is possible in more complex Sn-containing Zr alloys, both during exposure to irradiation (where the diffusion rates of solute species will be hugely accelerated) and during very long-term thermal ageing. However, spinodal decomposition is well known to make an important contribution to the properties of other nuclear alloys [28–31], and so this observation in these Zr alloys should be investigated as it can have important implications for the prediction of the mechanical properties in-service.

Acknowledgements

The atom probe facilities at the University of Oxford are funded by the EPSRC grants EP/M022803/1 and EP/T011505/1. STEM was performed using the 'South of England Analytical Electron Microscope' at the University of Oxford, supported by a UK Engineering and Physical Sciences Research Council (EPSRC) grant EP/K040375/1. The research used UKAEA's Materials Research Facility, which has been funded by and is part of the UK's National Nuclear User Facility and Henry Royce Institute for Advanced Materials. BMJ and JH would like to acknowledge funding from EPSRC program grant MIDAS (EP/S01702X/1) for the study of irradiation damage in zirconium alloys.

Bibliography

[1] A.T. Motta, A. Couet, R.J. Comstock, Annu. Rev. Mater. Res. 45 (2015) 311–343.
[2] C.E. Coleman, D. Hardie, J. Less-Common Met. 11 (1966) 168–185.
[3] J.B. Bai, C. Prioul, D. François, Metall. Mater. Trans. A 25 (1994) 1185–1197.
[4] J.E. Harbottle, F. Herbillon, J. Nucl. Mater. 90 (1980) 249–255.
[5] V.N. Shishov, M.M. Peregud, A. V. Nikulina, P. V. Shebaldov, A. V. Tselischev, A.E. Novoselov, G.P. Kobylyansky, Z.E. Ostrovsky, V.K. Shamardin, ASTM Spec. Tech. Publ. (2002) 758–778.
[6] A. V. Nikulina, V.A. Markelov, M.M. Peregud, V.N. Voevodin, V.L. Panchenko, G.P. Kobylyansky, J. Nucl. Mater. 238 (1996) 205–210.
[7] V.N. Shishov, A. V. Nikulina, V.A. Markelov, M.M. Peregud, A. V. Kozlov, S.A. Averin, S.A. Kolbenkov, A.E. Novoselov, ASTM Spec. Tech. Publ. 1295 (1996) 603–622.
[8] J. Ribis, S. Doriot, F. Onimus, J. Nucl. Mater. 511 (2018) 18–29.
[9] A. Harte, D. Jädernäs, M. Topping, P. Frankel, C.P. Race, J. Romero, L. Hallstadius, E.C. Darby, M. Preuss, Acta Mater. 130 (2017) 69–82.
[10] G. Sundell, M. Thuvander, P. Tejland, M. Dahlbäck, L. Hallstadius, H.O. Andrén, J. Nucl. Mater. 454 (2014) 178–185.
[11] T. Sawabe, T. Sonoda, J. Nucl. Sci. Technol. 55 (2018) 1110–1118.
[12] J. Eriksson, G. Sundell, P. Tejland, H.O. Andrén, M. Thuvander, J. Nucl. Mater. 550 (2021).
[13] A.C.P. Jain, P.A. Burr, D.R. Trinkle, Phys. Rev. Mater. 3 (2019) 33402.
[14] S. Yagnik, R.B. Adamson, G. Kobylyansky, J.H. Chen, D. Gilbon, S. Ishimoto, T. Fukuda, L. Hallstadius, A. Obukhov, S. Mahmood, ASTM Spec. Tech. Publ. STP 1597 (2018) 748–795.
[15] K. Thompson, D. Lawrence, D.J. Larson, J.D. Olson, T.F. Kelly, B. Gorman, Ultramicroscopy 107 (2007) 131–139.
[16] M.K. Miller, K.F. Russell, G.B. Thompson, Ultramicroscopy 102 (2005) 287–298.
[17] L.A. Giannuzzi, J.L. Drown, S.R. Brown, R.B. Irwin, F.A. Stevie, Microsc. Res. Tech. 41 (1998) 285–290.
[18] A.J. London, (2019) https://sourceforge.net/projects/atomprobelab/.
[19] A.J. London, Microsc. Microanal. (2019) 1–11.
[20] F. de la Peña, T. Ostasevicius, V.T. Fauske, P. Burdet, E. Prestat, P. Jokubauskas, M. Nord, K.E. MacArthur, M. Sarahan, D.N. Johnstone, J. Taillon, A. Eljarrat, V. Migunov, J. Caron, T. Furnival, S. Mazzucco, T. Aarholt, M. Walls, T. Slater, F. Winkler, B. Martineau, G. Donval, R. McLeod, E.R. Hoglund, I. Alxneit, I. Hjorth, T.

Henninen, L.F. Zagonel, A. Garmannslund, 5ht2, (2018).
[21] C.T. Rueden, J. Schindelin, M.C. Hiner, B.E. DeZonia, A.E. Walter, E.T. Arena, K.W. Eliceiri, BMC Bioinformatics 18 (2017) 529.
[22] A. Harte, M. Topping, P. Frankel, D. Jädernäs, J. Romero, L. Hallstadius, E.C. Darby, M. Preuss, J. Nucl. Mater. 487 (2017) 30–42.
[23] L. Yao, B. Gault, J.M. Cairney, S.P. Ringer, Philos. Mag. Lett. 90 (2010) 121–129.
[24] J.M. Hyde, M.K. Miller, M.G. Hetherington, A. Cerezo, G.D.W. Smith, C.M. Elliott, Acta Metall. Mater. 43 (1995) 3415–3426.
[25] A. Kwiatkowski Da Silva, D. Ponge, Z. Peng, G. Inden, Y. Lu, A. Breen, B. Gault, D. Raabe, Nat. Commun. 9 (2018) 1–11.
[26] J.E. Brown, G.D.W. Smith, Surf. Sci. 246 (1991) 285–291.
[27] G. He, Radiation Damage and Its Impact on Corrosion in Zirconium-Niobium Alloys - Thesis, University of Oxford, 2020.
[28] T. Yao, A.R. Wagner, X. Liu, A. El-Azab, J.M. Harp, J. Gan, D.H. Hurley, M.T. Benson, L. He, Materialia 9 (2020) 100592.
[29] F.A. Garner, J.M. McCarthy, K.C. Russell, J.J. Hoyt, J. Nucl. Mater. 205 (1993) 411–425.
[30] F.A. Garner, H.R. Brager, R.A. Dodd, T. Lauritzen, Nucl. Inst. Methods Phys. Res. B 16 (1986) 244–250.
[31] K. Nakai, C. Kinoshita, J. Nucl. Mater. 169 (1989) 116–125.